

Application of CALPHAD to high pressures

Eli Brosh^{a,b,*}, Guy Makov^b, Roni Z. Shneck^a

^a Department of Materials Engineering, Ben-Gurion University of the Negev, P.O. Box 653, Beer-Sheva 84105, Israel

^b NRCN, P.O. Box 9001, Beer-Sheva 84190, Israel

Received 10 October 2006; received in revised form 9 December 2006; accepted 21 December 2006

Available online 7 February 2007

Abstract

The current methods of performing CALPHAD (CALculation of PHase Diagrams) calculations of high-pressure phase equilibria often lead to spurious predictions of negative thermal expansion or negative heat capacity at high pressures. It is shown that the origin of the problem lies in an incompatibility between the temperature dependence of the widely used SGTE (Scientific Group Thermodata Europe) database and that of typical equations of state of the Mie–Grüneisen type. This inconsistency is also linked to the general problem of describing mechanical instability in CALPHAD. In the present work, a new free energy formulation is developed specifically for inclusion of pressure effects in CALPHAD methodology. It is based on an interpolation between SGTE data at low pressures and the quasiharmonic lattice model at high pressures. The new formulation is constrained to physically credible predictions of the thermophysical properties, while preserving the simplicity of the CALPHAD method. Examples are given of calculations of thermophysical properties and high-pressure phase equilibria in Al, Si, MgO, Fe and the Al–Si binary alloy system.

© 2007 Elsevier Ltd. All rights reserved.

Keywords: Thermodynamic; Modelling; Pressure; Phase diagram; Equation of state

1. Introduction

The CALPHAD methodology has been very successful in the coupling of thermochemistry and phase equilibria in multicomponent systems at ambient pressure. However, up to now there have been only a few attempts to include pressure effects on condensed phases in CALPHAD calculations. The motivation for such attempts stems mainly from interest in geophysical problems [1] and high-pressure materials physics. In addition there is, in recent years, an interest in extending the CALPHAD method to problems including volume thermal expansion [2,3]. Ideally, it would be best to treat the volumetric data as part of consistent thermodynamic modelling of pressure effects on the Gibbs free energy rather than as a separate database.

In CALPHAD, the Gibbs free energy is written explicitly as a function of temperature and pressure (T, P). Thus, the natural

way to extend the formalism to high pressure is to write:

$$G(T, P) = G(T, P_0) + \int_{P_0}^P V(T, P') dP' \quad (1)$$

where G is the Gibbs free energy and P_0 is the reference pressure (usually 1 atm). The first term in Eq. (1) is the Gibbs free energy along the reference isobar, which is the standard CALPHAD data. It should be noted that $G(T, P_0)$ is not a mere tabulation of experimental data since for many calculations, it is necessary to extrapolate $G(T, P_0)$ beyond the measured range. e. g. as done in SGTE (Scientific Group Thermodata Europe) databases [4].

The calculation of the integral in Eq. (1), requires an EOS (Equation Of State): $V(T, P)$. Most of the attempted high-pressure CALPHAD calculations employed for condensed phases the Murnaghan EOS [5,6] with temperature-dependent parameters $V_0(T)$, $B_0(T)$, $B'_0(T)$ that are the volume, the bulk modulus and its first pressure derivative, taken at the reference pressure. Other EOS with similar parameterizations were also considered for application in CALPHAD databases, namely the Birch–Murnaghan EOS [7] and the Jacobs–Oonk EOS [8,9].

* Corresponding author at: Department of Materials Engineering, Ben-Gurion University of the Negev, P.O. Box 653, Beer-Sheva 84105, Israel. Tel.: +972 8 6104887; fax: +972 8 6104887.

E-mail address: ebrosh@nana.co.il (E. Brosh).

However, up to now the application of CALPHAD at high pressures may be considered as unsuccessful, because the existing models often give manifestly wrong predictions of high-pressure thermophysical properties. For example, negative heat capacities at high pressure have been predicted for MgO and iron [9] as well as for molybdenum [10]. In addition, Jacobs and Oonk [8] have shown that existing models are prone to predicting negative thermal expansion at high pressures,¹ even for close-packed substances, where such phenomena are not expected. It is obvious that the failure of the high- P high- T predictions must arise either from a fault in the structure of the EOS or from some incompatibility between the CALPHAD methodology and the EOS in question.

In the present work, we attempt to resolve this issue and propose a practical formalism for high-pressure calculations in CALPHAD.

First, we try to replace the temperature-dependent Murnaghan EOS by the more established Mie–Grüneisen formulation. As will be seen in Section 2, such a substitution does not resolve the problematics if we retain the usual CALPHAD databases for the ambient pressure caloric properties in $G(T, P_0)$. In Section 3, we propose a new formulation for the inclusion of pressure effects in CALPHAD methodology. In Section 4, this new formulation is applied to the thermodynamic modelling of the elements Al, Si and Fe, the compound MgO and to the Al–Si binary alloy system.

2. Use of the Mie–Grüneisen EOS in CALPHAD

One of the possible sources of the problematics in the current modelling of pressure effects in CALPHAD is the use of completely empirical EOS formulations. Thus, it may seem that an improvement can be achieved if an EOS based on physical considerations is invoked instead. For example, consider the MG (Mie–Grüneisen) EOS [11], which is commonly used to describe the thermal contribution to the high-pressure behaviour of condensed matter:

$$P = P_c(V) + \frac{\gamma}{V} \cdot [E(T, \theta_D) - E(T_0, \theta_D)] \quad (2)$$

where $P_c(V)$ is the cold compression curve (the T_0 isotherm) and the second term is the thermal pressure [11]. γ is the Grüneisen parameter, $E(T, \theta_D)$ is the internal energy, evaluated from the standard expression in the Debye model and θ_D is the Debye temperature that is a function of volume. The MG EOS has several advantages over the more empirical approach that was previously tried in CALPHAD. For example, if the γ parameter is kept positive, negative thermal expansion is avoided at any pressure.

Hänström and Lazor [12] fitted an MG type EOS to wide-ranging experimental data for aluminium. While Hänström and Lazor treated only the P – V – T relation, here, we use their fitted EOS to examine the effect of pressure also on “caloric” properties. Hence, using their fitted EOS, the Gibbs

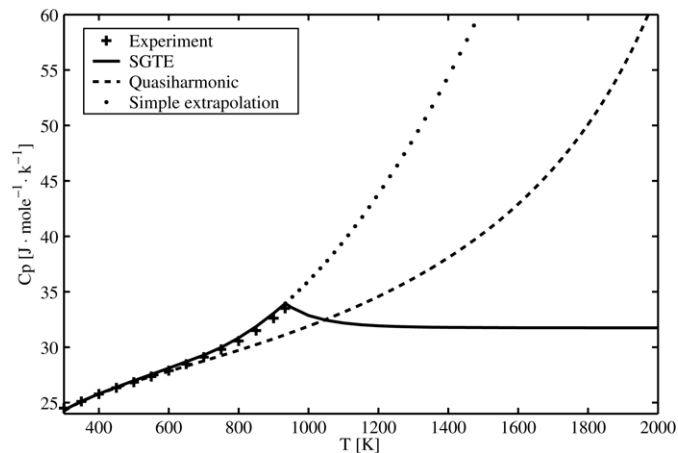


Fig. 1. The calculated isobaric heat capacity of fcc-Al at ambient pressure. The solid curve corresponds to the SGTE database. The broken curve corresponds to a calculation made with the quasiharmonic model for C_v and the Mie–Grüneisen EOS. The dotted curve corresponds to a simple polynomial extrapolation of the solid heat capacity beyond the melting point. Measured heat capacity is indicated by crosses.

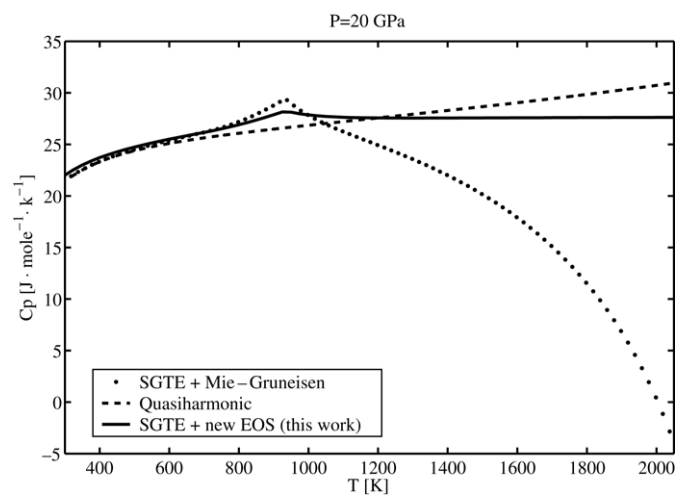


Fig. 2. The calculated isobaric heat capacity of fcc-Al at 20 GPa. The dotted curve corresponds to a combination of the SGTE data for ambient-pressure heat capacity and the Mie–Grüneisen EOS (2). The broken curve corresponds to a calculation made with the quasiharmonic model for C_v and the Mie–Grüneisen EOS. The solid curve corresponds to the new EOS developed in the present work.

free energy of solid aluminium can be calculated by Eq. (1), with the $G(T, P_0)$ term taken from the SGTE database [4] and the pressure-dependent term is calculated (numerically) using Eq. (2). In particular, let us consider the effect of pressure on the isobaric heat capacity calculated in this manner.

The heat capacity at ambient pressure as given in the SGTE database, is shown in Fig. 1, where it is seen to match the experimental data [13] below the melting point. However, at $P = 20$ GPa, the heat capacity calculated by combining the SGTE database for ambient pressure and the MG EOS (2) is manifestly unphysical. As seen in Fig. 2, this combination yields a negative heat capacity above $T = 2000$ K, a temperature that is below the melting point at $P = 20$ GPa [12].

¹ This spurious anomaly is equivalent to anomalous pressure-dependence of the entropy [8].

A different method to calculate the high-pressure isobaric heat capacity is to use the quasiharmonic model that is the basis of the MG EOS [11] i.e. the standard Debye expression is used for the isochoric heat capacity $C_V(T, \theta_D)$. The isobaric heat capacity is found from the thermodynamic identity:

$$C_p - C_v = -T \cdot \left[\left(\frac{\partial V}{\partial T} \right)_P \right]^2 \cdot \left(\frac{\partial P}{\partial V} \right)_T \quad (3)$$

where the right hand side is derived from Eq. (2). This ensures the thermodynamic consistency between the calculated C_p and the EOS. $C_p(T)$ at ambient pressure calculated by the quasiharmonic model is shown in Fig. 1, where it is somewhat lower than the experimental data (Hänström and Lazor did not fit their EOS to heat capacity data). However, as seen in Fig. 2, at $P = 20$ GPa, the quasiharmonic model together with the MG EOS exhibits physically acceptable behaviour, much better than the unphysical prediction that was obtained when the MG EOS was used together with the SGTE database.

Thus, we conclude that the unphysical predictions that are obtained when the MG EOS is used in combination with the SGTE database do not originate in the EOS itself. Rather, these problems are a symptom of *incompatibility* between the MG EOS and the standard CALPHAD modelling, namely, between the two terms in Eq. (1).²

The origins of this incompatibility may be traced by looking again at Fig. 1. It is seen that the measured heat capacity increases monotonically with temperature, with at least the first two derivatives being positive. The quasiharmonic model reproduces this feature, up to and also above the melting temperature, much like a simple polynomial extrapolation of the experimental results. This behaviour is obvious if one considers that according to the quasiharmonic model, C_V reaches a constant value at high temperature (the Dulong–Petit heat capacity) whereas the EOS predicts that the right hand side of Eq. (3) is rising monotonically. In the SGTE database, on the other hand, the heat capacity of the solid phase above the melting point decreases until it converges to a fixed value, in contradiction with the quasiharmonic model.

The rationale behind the extrapolation used in the SGTE database, is to avoid the reappearance of solid phases at high temperatures [14]. Indeed, it is seen in Fig. 3, that when a simple polynomial extrapolation is used for the heat capacity of the solid (and the measured heat capacity for the liquid), the solid phase reappears at high temperature. The quasiharmonic model is similar to the simple polynomial extrapolation in that it predicts a decrease, with the rise of temperature, in the magnitude of the difference between the Gibbs energies of the solid and the liquid. However, reappearance of the solid at high temperature is avoided because the Mie–Grüneisen EOS predicts that the solid becomes mechanically unstable at high temperatures. While several mechanical instabilities are

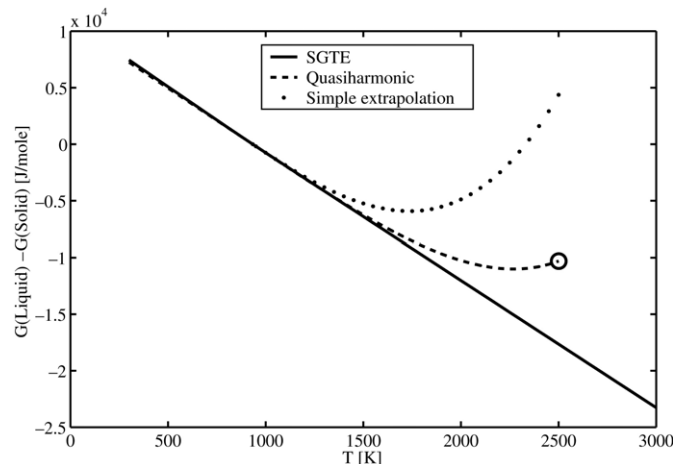


Fig. 3. The Gibbs free energy difference between liquid and solid phases of aluminium. The three curves correspond to the SGTE database, the quasiharmonic model and a simple polynomial extrapolation of the heat capacity. The simple polynomial extrapolation results in a reappearance of the solid phase around $T = 2400$ K. The quasiharmonic+MG calculation does not predict such a reappearance because the MG EOS predicts a mechanical instability at $T = 2450$ K (marked by a circle in the figure).

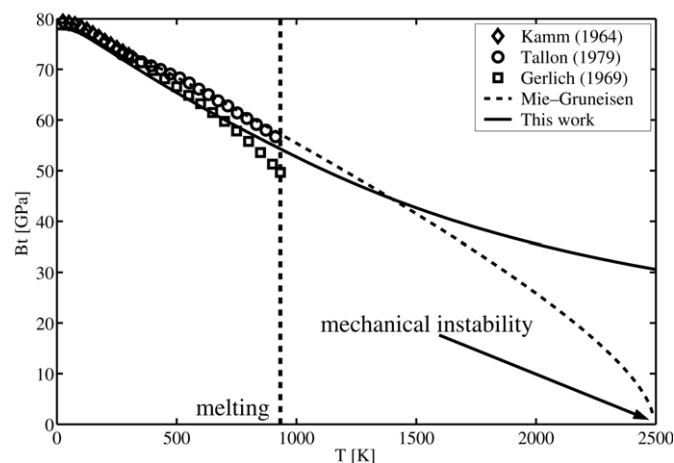


Fig. 4. The temperature dependence of the isothermal bulk modulus of solid aluminium at ambient pressure. The Mie–Grüneisen EOS predicts a mechanical instability at 2450 K where the bulk modulus decreases below zero. The calculation done with our new formalism does not predict a mechanical instability.

possible [15], the mechanical instability that is deduced from the P – V – T relation is the spinodal instability [16,17] i.e. the decrease of the bulk modulus below zero, as shown in Fig. 4.

Current CALPHAD methodology does not take into account the possibility of a mechanical instability [15,18]. If mechanical instabilities were incorporated in CALPHAD methodology, the complex extrapolation scheme that SGTE uses for heat capacities would not be required, and the incompatibility with the quasiharmonic model would be removed. While the neglect of mechanical instabilities greatly simplifies the thermodynamic description of many phases, it prevents the direct application of theoretically calculated lattice stabilities in CALPHAD [18]. Here we have shown that the neglect of mechanical instabilities also prevents the use of the physically

² $C_p = C_p(T, P_0) + \Delta C_p(T, P)$ where the first term is the ambient pressure heat capacity taken from the SGTE database and the second term is the pressure-dependent contribution, calculated using the EOS. The negative value of C_p arose from the incompatibility between these two terms.

derived MG EOS in CALPHAD modelling of pressure effects.

3. A new EOS for use in CALPHAD

In Section 2, we saw that the attempt to invoke the physically derived MG EOS in the CALPHAD scheme fails. The origin of this failure is traced to an incompatibility between the heat capacity in the SGTE database (on which most of the current CALPHAD calculations are based) and the quasiharmonic model from which the Mie–Grüneisen EOS is derived. This incompatibility was also linked to the general problem of treating mechanical instability in current CALPHAD methodology.

Therefore, there are several routes to the modelling of pressure effects in CALPHAD.

- Remaking of the CALPHAD thermodynamic databases in such a manner that they become compatible with a physically derived EOS, as in the recent work of Jacobs et al. [19].
- Developing a new empirical EOS model that is compatible with the current CALPHAD methodology, but is physically acceptable. Namely, negative heat capacities and negative thermal expansion are to be avoided.
- Giving up the ambition to treat phase equilibria and thermophysical properties in the unified framework of a Gibbs free energy model. Instead, the Gibbs free energy model will be used just for calculating the phase diagram. Thermophysical properties such as molar volume and bulk modulus will be treated in a separate database in which one may use a physically derived EOS.

Here we follow route (b), although it should be acknowledged only as an interim solution, since our opinion is that route (a) should be taken eventually.

At low pressures, we propose to continue using the current CALPHAD methodology with an interpolation to the quasiharmonic model at high pressures. Thus we shall retain the successful features of the present formalism as well as its databases while preventing its unphysical predictions at high pressure.

We propose the following Gibbs free energy scheme for use in CALPHAD:

$$G(T, P) = G_c(P) + G^{QH}(T, P) - [G^{QH}(T, P_0) - G(T, P_0)] \cdot I(P). \quad (4)$$

The first term accounts for the cold compression curve: $G_c(P) = \int_{P_0}^P V(T_0, P') dP'$ and $G(T, P_0)$ is the Gibbs free energy on the reference isobar.³ $I(P)$ is a dimensionless and monotonically decreasing interpolation function with the limiting values $I(P_0) = 1$ and $I(\infty) = 0$.

The function $G^{QH}(T, P)$ is given by:

$$G^{QH}(T, P) = 3NR \cdot T \cdot \ln \left[1 - \exp \left(-\frac{\theta(P)}{T} \right) \right] \quad (5)$$

³ Here, we use $(T = 0 \text{ K}, P = P_0)$ as a reference state for both $G(T, P_0)$ and $G(T, P)$.

where N is the number of atoms per unit of molecular formula, θ is the Einstein temperature. Here, θ is increasing with pressure and independent of temperature,⁴ following a concept that we borrowed from Gerya et al. [20].

Although $G^{QH}(T, P)$ resembles the quasiharmonic model, as implied by the superscript QH, its meaning is somewhat different. Note that Eq. (5) is written for the Gibbs free energy whereas in the quasiharmonic model the Helmholtz free energy is modelled by an expression that is similar to (5). As result, the isobaric heat capacity calculated from $G^{QH}(T, P)$ is lower than $3NR$ and than the isobaric heat capacity calculated from the quasiharmonic model as well as than the actual isobaric heat capacity.⁵ However, at high pressures, the difference between the isobaric and the isochoric heat capacities becomes negligible. In addition, at high pressure, there is little difference between the dependence of θ on pressure and the corresponding volume dependence of characteristic temperatures in the quasiharmonic model. This is true because at high pressures, thermal expansion is small, so that the volume depends just on the pressure.

Thus, at high pressure $G^{QH}(T, P)$ is a fair approximation of the quasiharmonic model so that the temperature effects in Eq. (4) may be viewed as an interpolation between $G(T, P_0)$ at ambient pressure and the quasiharmonic model at high pressure.

Note that the proposed scheme implies a monotonic decrease of the heat capacity from its value at $P = P_0$ to the quasiharmonic $C_P^{QH}(T, P)$ at high pressure. *The heat capacity cannot become negative* because $C_P^{QH}(T, P)$ is a positive lower bound.

The contribution of the QH term to the volume is given by:

$$V^{QH}(T, P) = \frac{\partial G^{QH}(T, P)}{\partial P} = 3NR \cdot \frac{\exp(-\frac{\theta}{T})}{1 - \exp(-\frac{\theta}{T})} \cdot \frac{d\theta}{dP} \quad (6)$$

where it may be verified that $V^{QH}(T = 0, P) = 0$.

Note that since $\frac{d\theta}{dP} > 0$, $V^{QH}(T, P)$ results in a definite positive contribution to the volume and to the thermal expansion.

The square-bracketed term in Eq. (4) arises from the difference between the actual heat capacity at normal pressure $C_P(T, P_0)$ and the heat capacity that is contributed by the $G^{QH}(T, P_0)$ term at the same conditions $C_P^{QH}(T, P_0)$:

$$C(T) = G^{QH}(T, P_0) - G(T, P_0) = \int_0^T dT' \int_0^{T'} dT'' \cdot \frac{1}{T''} [C_P(T'', P_0) - C_P^{QH}(T'', P_0)]. \quad (7)$$

⁴ This is different from the conventional quasiharmonic model where the characteristic temperatures are functions of volume as $\Theta_D(V)$ rather than of pressure.

⁵ Provided that the Einstein temperature $\theta(P = P_0)$ is not mistakenly taken to be too low.

Now, since $C_P^{\text{QH}}(T, P_0)$ is lower than the actual heat capacity, the function $C(T)$ is positive as well as its two first derivatives: $C(T) > 0$, $\frac{dC(T)}{dT} > 0$, $\frac{d^2C(T)}{dT^2} > 0$ and the volumetric contribution of the interpolation term

$$V^{\text{Interp}}(T, P) = -C(T) \cdot \frac{dI(P)}{dP} \quad (8)$$

is positive and makes a positive contribution to the thermal expansion. Thus, negative thermal expansion is avoided in our model, with little regard to the particular choice of model parameters.

The functions $G_c(P)$, $\theta(P)$, $C(T)$ and $I(P)$ that are suggested for use in the model are given in [Appendices A–D](#). However, the choice of these functions is not unique and the validity of the concept does not depend on the details of their particular formulation.

3.1. Limitations of the proposed model

As explained above, the new model is designed specifically for application within the current CALPHAD methodology. This results in some problematic features.

One limitation of the model is the underestimation of the heat capacity at high temperatures that results from the reliance on SGTE-type extrapolation of the heat capacity. As seen in [Fig. 1](#), at high temperature the SGTE heat capacity is significantly lower than the heat capacity calculated from the quasiharmonic model. Also, in [Fig. 2](#) it is seen that while our model predictions for the high-pressure heat capacity of aluminium are quite reasonable, they are lower than the quasiharmonic calculation at high temperature. Similarly, it is possible to show that the high-temperature thermal expansion is also underestimated by the proposed model.

A second important limitation is the overestimation of the bulk modulus at high temperatures. In [Fig. 4](#), the isothermal bulk modulus of solid aluminium at ambient pressure, as calculated with the new EOS is compared with experimental results as well as with the corresponding calculation using the MG EOS. It is seen that the extrapolation of the bulk modulus to high temperature is very different from the MG EOS. Namely, our new EOS does not predict the decrease of the bulk modulus to zero at $T = 2450$ K. Instead, with the new EOS, the bulk modulus converges at high temperatures to a constant positive value (see [Appendix D](#)). Thus, the proposed EOS avoids mechanical instability, in line with the current CALPHAD methodology. A necessary consequence of this CALPHAD-compatibility is that our EOS predicts a concave temperature-dependence of the bulk modulus $\frac{\partial^2 B}{\partial T^2} > 0$ at high temperature. This is an unphysical feature since a linear or convex temperature dependence is observed in experiments, as well as in calculations using the MG EOS. However, as may be seen in [Fig. 4](#), the calculated concavity of the $B(T)$ function is quite mild, so that this error in the sign of the fourth-order derivative of the Gibbs free energy $\frac{\partial^4 G}{\partial P^2 \partial T^2}$ should be tolerable for most purposes.

Finally, it should be understood that the new EOS, as detailed in the preceding sections, is intended for modelling

“normal” materials. For example, it does not include magnetic effects on the EOS. However, the standard approach in CALPHAD is to describe the magnetic contribution by a separate, “magnetic” term in the Gibbs free energy function [4, 9]. Magnetic effects on the EOS can be described by making this term pressure dependent [9], while only non-magnetic Gibbs free energy is used for calculating the $C(T)$ function in our model.

The modelling of anomalies such as negative thermal expansion or positive $\frac{\partial B}{\partial T}$ is not to be done by just finding a suitable set of EOS parameters.⁶ Instead, the modelling of anomalous properties with the proposed EOS would require a more explicit physical description. E.g. in [Section 4.2](#) we apply the two-state model [20,21], for modelling the anomalous thermophysical properties of liquid silicon.

4. Applications

In the preceding section, a new free energy formulation was introduced, specifically designed for high-pressure calculations in CALPHAD. In [Sections 4.1–4.4](#), the fitting of the EOS parameters to experimental and theoretical information on the elements Al, Si and Fe and the oxide MgO is discussed.

The fitted model parameters and some additional information needed for the application of the model are given in [Tables 1–3](#). Nine adjustable EOS parameters were used for each phase.⁷ Among these parameters, the Einstein temperature θ had only a small effect on the fitting. It was usually estimated and left unchanged. Where possible, the parameters V_0 , B_0 , B'_0 were fitted to room-temperature compression results. The Grüneisen parameter γ_0 was fitted to data on thermal expansion at ambient pressure and moderate temperatures. The parameters δ_0 , δ_1 and b_1 were fitted to available information on the temperature dependence of the bulk modulus and high-temperature thermal expansion.⁸ The parameter b_0 affects the thermophysical properties only at high pressure, hence, it was usually left at its default value of $b_0 = 1$. Where only scarce thermophysical data was available, the EOS parameters were first estimated on the basis of better-known phases and then adjusted to account for known phase equilibria.

In [Section 4.5](#), the new EOS with fitted parameters is utilized for the calculation of pressure effects on the Al–Si phase diagram. Throughout the present section, the aim is to examine the proposed model rather than to produce a definitive assessment of the substance under examination. Hence, wherever possible, the $G(T, P_0)$ functions were taken from the SGTE database [4] without attempting to improve them. The calculations were performed using Thermo-Calc [22].

⁶ While positive thermal expansion is a feature of the basic construction of the model (see the previous section), the decrease of the bulk modulus with temperature is determined by the particular choice of the functions $\theta(P)$ and $I(P)$. With the functions that were chosen here, any reasonable set of parameters will lead to $\frac{\partial B}{\partial T} < 0$. See Eqs. (B.4) and (D.4).

⁷ The coefficients c_n are not adjustable parameters as explained in [Appendix A](#).

⁸ The parameter b_1 was adjusted manually. Its default value was set to $b_1 = 1$.

Table 1
Fitted EOS parameters

		V_0 (cc/mol)	B_0 (GPa)	B'_0	c_2	c_3	c_4	c_5	θ (K)	γ_0	δ_0	b_0	δ_1	b_1
Al	fcc	9.9	78	4.3	−0.10929	0.86175	−0.60167	0.84920	300	2.1	6	1	9	1
	Liquid	10.55	68	4.7	−0.18399	1.1335	−0.74470	0.79516	300	2	6	1	10	1
Si	diamond	12	100	4	−0.25211	1.5381	−1.3453	1.0593	500	0.38	7	1	15	1
	β -Sn	9.5	75	4	0.052675	0.2936	−0.19216	0.90012	500	0.4	7	1	10	1
	sh	9.446	75	4	0.05801	0.21707	−0.17329	0.89821	500	0.6	7	1	10	1
	hcp	9	70	4	0.13307	−0.088527	0.067916	0.88754	500	1.78	7	1	10	1
	fcc	8.96	70.07	4	0.13711	−0.10538	0.082126	0.88614	500	1.78	7	1	10	1
	Liquid.Si ¹	12	100	4	−0.25211	1.5381	−1.3453	1.0593	500	0.38	7	1	15	1
	Liquid.Si ²	9.51	66	4	0.10325	0.041045	−0.052367	0.90807	500	1.78	7	1	10	1
MgO	Solid	11.2	166	4.15	−0.029216	0.47353	−0.15766	0.71334	570	1.57	4.5	1	15	1
Fe	bcc	7.05	170	6.2	−0.18261	1.1197	−0.71573	0.77861	300	1.55	6	1	15	3
	fcc	6.826	140	8	−0.30848	1.6444	−1.1570	0.82100	250	2	4	1	10	3
	hcp	6.677	170	5.5	0.013989	0.22860	0.18829	0.56912	250	2.85	6	0.7	10	5.5
	Liquid	7.06	140	5.8	−0.021997	0.38136	0.05388	0.58675	250	2.1	6	1	15	3

Table 2
Fitted lattice stabilities for silicon phases

Phase	Ambient pressure lattice stability (J/mole)
β -Sn	$G(\text{diamond}) + 27\,000 - 3.2 \cdot T$
Simple hexagonal	$G(\text{diamond}) + 27\,900 - 3.85 \cdot T$
Liquid.Si ¹	$G^{\text{SGTE}}(\text{Liquid}) - 14617.48 + 12.8 \cdot T$
Liquid.Si	$G(\text{Si}^1) + 1600 \cdot R - 1.3 \cdot R \cdot T$

Table 3
Interaction parameters in the Al–Si system

Parameter	Value (J/mole)
$0L_{\text{Si}^1,\text{Si}}$	25 000
$0L_{\text{Si}^1,\text{Al}}$	25 000

4.1. Aluminium

The data for fitting the EOS parameters of aluminium was taken from Refs. [12,23–34]. In Fig. 4, the calculated and the experimental results [27,28] for the isothermal bulk modulus of the solid phase are compared. It is seen that the calculation is fairly close to the experimental points up to the melting point. In Fig. 5, the calculated zero-pressure molar volume is compared with the experimental results of Touloukian [23] (for the solid), Sarou-Kanian et al. [31] and Gathers [34] (at $P = 0.24$ GPa). The calculated phase diagram of aluminium is shown in Fig. 6, along with the experimental data of Boehler and Ross [32] and Hänström and Lazor [12]. The theoretical (model-potential) calculations of Pélissier [33] that were given only a small weight in fitting the EOS parameters, are also shown in Fig. 6.

Hugoniot data was not used for fitting the EOS parameters so that the comparison of the calculated Hugoniot with experiment may serve to test the proposed model. In Fig. 7 the calculated Hugoniot is compared with the experimental P – V Hugoniot curve, taken from a recent compilation [35]. A fair agreement

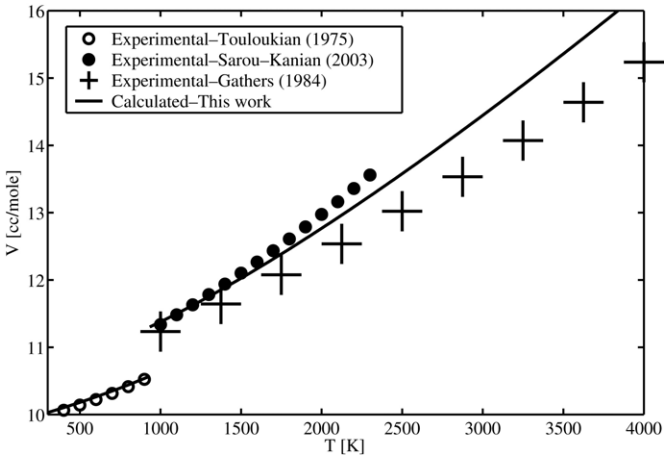


Fig. 5. The calculated molar volume of aluminium compared with experimental data.

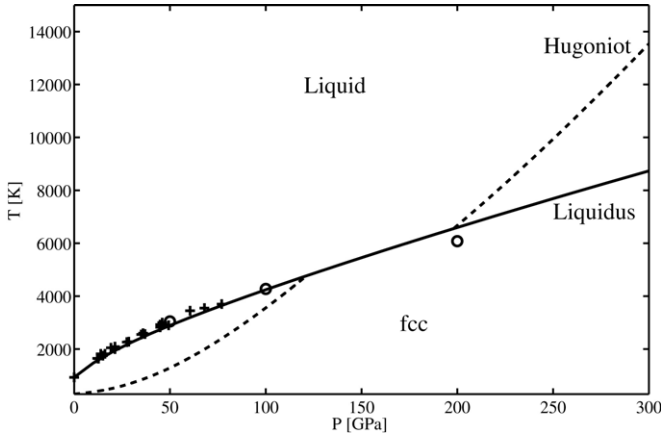


Fig. 6. The phase diagram and the principal Hugoniot of aluminium in P – T coordinates. The liquidus is compared with the experimental data [12] (smaller crosses) and with a theoretical calculation [33] (circles). The onset of melting on the Hugoniot is calculated at $P = 120$ GPa and the end of melting is calculated at $P = 200$ GPa.

with experiment is observed up to the enormous pressure of 2 TPa.

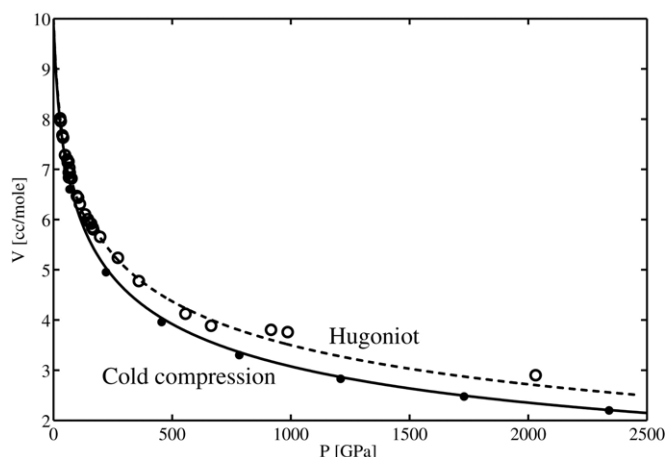


Fig. 7. The cold compression curve (solid curve) and the principal Hugoniot (broken curve) of aluminium, calculated in this work. The cold compression curve is compared with the theoretical calculation of Chubin et al. [25]. The experimental data for comparison with the calculated Hugoniot is taken from Ref. [35].

The calculated Hugoniot curve in P – T coordinates is shown in Fig. 6. The calculated onset of melting on the Hugoniot is at $P = 120$ GPa. This is not far from the corresponding experimental value of $P = 130$ GPa, reported by Shaner et al. [36]. However, the calculation also predicts the complete melting on the Hugoniot at around $P = 200$ GPa. This result differs from the corresponding value of $P = 150$ GPa that may be inferred from Shaner et al. measurements⁹ [36]. The discrepancy may be due to an overestimation of the melting enthalpy at high pressures and high temperature, which may result from our use of the SGTE extrapolation of the heat capacity.

4.2. Silicon

The experimental data for fitting the EOS parameters of silicon was taken from references [37–45]. In the present work, only the diamond, β -Sn, sh (simple hexagonal), hcp and fcc phases were modelled. The phase Si_{XI} [45] that lies between the β -Sn and the fcc and the intermediate phase Si_{VI} between the sh and hcp [41] are not modelled because of insufficient information on these phases. For the β -Sn and sh (simple hexagonal) phases, of silicon, it was necessary to evaluate the lattice stability, relying on theoretical calculations [46,47].

Liquid silicon exhibits some anomalies, similar to water [48]. Particularly, the sound velocity of liquid silicon increases with temperature [44] instead of decreasing as in normal substances. This anomaly makes the modelling of liquid silicon difficult, since our basic formulation is intended for modelling of “normal” substances. Therefore, for modelling liquid and amorphous silicon we used a two-state model, which is closely related to the model proposed by Deb et al. [49,50] to account for pressure-induced amorphization in silicon. Two species were defined for liquid silicon: semiconducting Si^1 and ordinary (metallic) liquid Si. For the Si^1 , we used the EOS

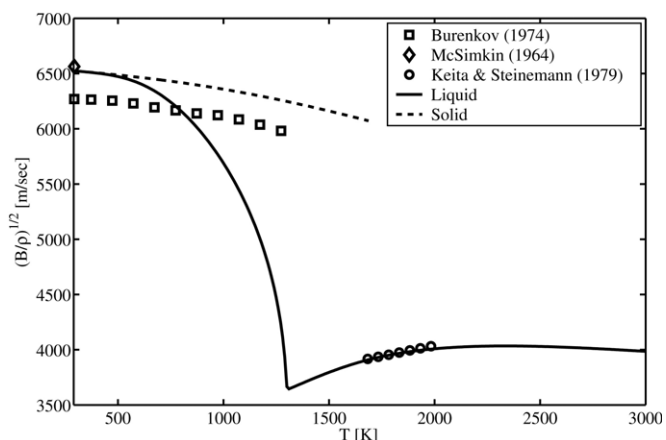


Fig. 8. Modelling of the anomalous sound velocity in liquid silicon. The rise of sound velocity with temperature is reproduced. For comparison, the quantity $c_B = (B_s/\rho)^{1/2}$ is plotted also for the solid (diamond phase) silicon. At low temperatures the amorphous silicon behaves much like the semiconducting diamond phase. Around $T = 1350$ K, the model depicts a transition between semiconducting and metallic states of liquid Si. Above the melting point, the anomalous rise of the sound velocity with temperature is reproduced.

parameters of the diamond-phase silicon. The ambient-pressure lattice stability of both liquid silicon species, as well as the EOS parameters of the ordinary (metallic) liquid Si, were fitted to the experimental results [44,43]. Following Deb et al. [49], we assigned a repulsive (positive) interaction parameter between the two species of liquid Si, so that the transition between them takes place in a narrow temperature range.

The calculated and the experimental sound velocity in liquid silicon are plotted in Fig. 8. It is seen that the anomalous temperature-dependence of the sound velocity is reproduced by our model. The quantity $c_B = (B_s/\rho)^{1/2}$ where B_s is the adiabatic bulk modulus and ρ is the density is equal to the sound velocity only above the melting point. However, in Fig. 8, c_B is plotted down to room temperature, so that it is seen that the calculated properties of the supercooled liquid/amorphous phase, resemble those of normal diamond-structured silicon. This feature is in line with both measurements and calculations of amorphous silicon [51].

The calculated P – T phase diagram of silicon is shown in Fig. 9. It is important to note that the calculation is based on a relatively small amount of experimental data. The steep negative slope of the diamond/ β -Sn equilibrium line is fitted to experiment while the similar slope of the β -Sn/sh line is estimated based on the experiments of Voronin et al. [45]. The small negative slopes of the sh/hcp and the hcp/fcc lines are a result of the use of SGTE lattice stabilities for fcc and hcp in the present calculation. The high-pressure liquidus may be regarded as not much more than a guess.

4.3. MgO

The EOS parameters for MgO (periclase) were fitted to experimental data on molar volume and thermal expansion at

⁹ Shaner et al. [36] measurements for aluminium ended at $P = 150$ GPa.

¹⁰ Duclos et al. found that the transition to hcp occurs at $P = 41.8$ GPa. The pressure range 37.6–41.8 GPa corresponds to the stability of an intermediate phase, between sh and hcp, which was not modelled in the present work.

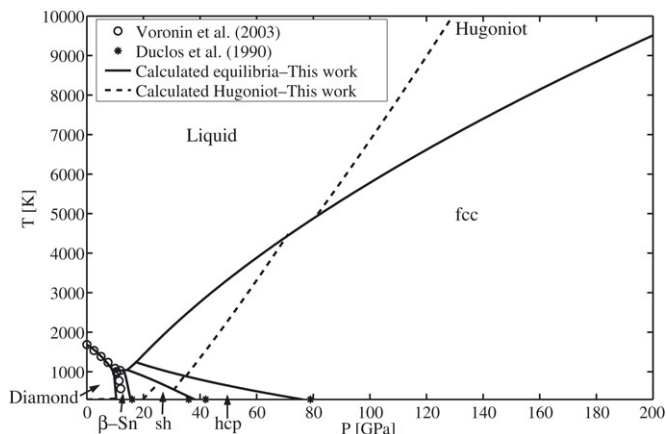


Fig. 9. The calculated P - T phase diagram and the Hugoniot curve of silicon. At room temperature, the calculated phase-transition pressures are $P = 10.4$ GPa for diamond- β -Sn, $P = 15.5$ GPa for β -Sn-sh, $P = 38.1$ GPa for sh-hcp and $P = 76.3$ GPa for hcp-fcc. These values are quite close to the corresponding experimental results i.e. $P = 10.5$ – 13.4 GPa [45], $P = 16$ GPa [41], $P = 37.6$ – 41.8 GPa [42]¹⁰ and $P = 79 \pm 2$ GPa [42].

ambient pressure [52], adiabatic bulk modulus [53] and room-temperature compression [54].

The volume thermal expansion coefficient of MgO, calculated at various pressures, is shown in Fig. 10, alongside the ambient-pressure measurements of Dubrovinsky and Saxena [52]. Also presented in the figure are the results of two model-calculations of the thermal expansion at high pressure [55,56], both are which are derived from the MG EOS. The agreement between our calculation and the other models regarding the thermal expansion at high pressure shows that at high pressures, our CALPHAD-compatible formulation is very similar to the better-established MG EOS. The present model does not use a direct fit of the ambient-pressure thermal expansion as an input. Rather, the temperature dependence of the thermal expansion is constrained by the $C(T)$ function that is not fitted to volumetric data. Hence, the fitting of ambient-pressure thermal expansion is non-trivial. For MgO, the difference between calculation and the experiment reaches 5% at $T = 3000$ K.

The calculated pressure-dependence of the heat capacity at $T = 2300$ K is shown in Fig. 11, where the predictions of our EOS are compared with those of Jacobs and Oonk [8] and Lu et al. [9]. Our model predicts a monotonic decrease of the heat capacity with the increase of pressure whereas the model of Jacobs and Oonk [8] results in an increase of the heat capacity with pressure. The model of Lu et al. [9] predicts negative heat capacity of MgO above 50 GPa, as if the phase becomes unstable with respect to entropy fluctuations. Clearly, the behaviour that is predicted by our model is more physical.

4.4. Fe

The data for fitting the EOS parameters of iron was taken from references [9,23,57–67]. Only the bcc, fcc and hcp phases were included in this preliminary assessment. The controversial β -Fe was not modelled, however, following Anderson and Isaak [68] it was assumed to be very similar to hcp with

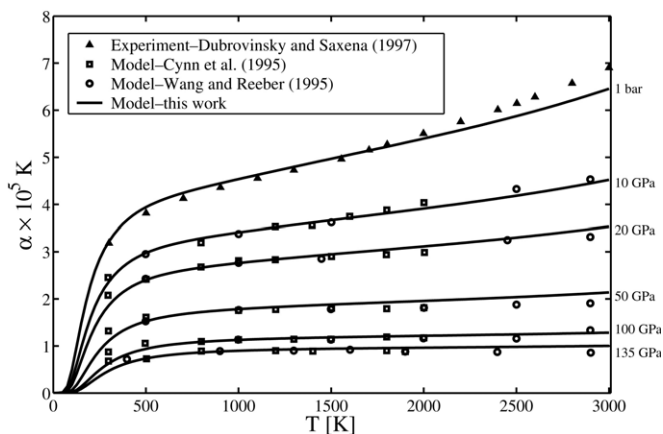


Fig. 10. The volume thermal expansion coefficient of MgO, calculated in this work for various pressures, is shown alongside the ambient-pressure experimental results of Dubrovinsky and Saxena [52] and other model calculations.

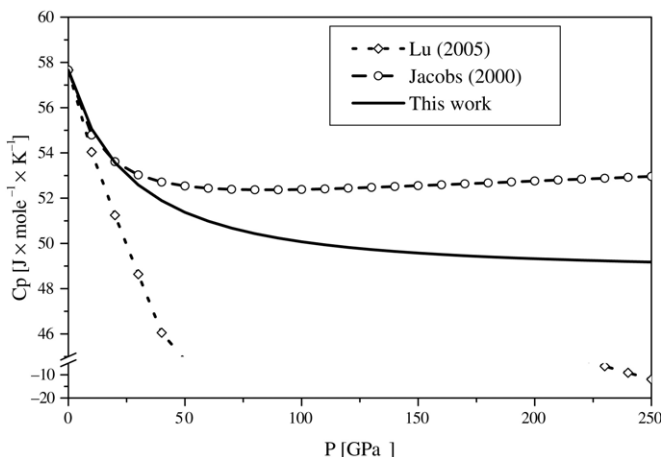


Fig. 11. The variation of heat capacity with pressure as calculated in the present work, in comparison with two other models proposed for use in CALPHAD. While our model gives a monotonically decreasing heat capacity, the other models [8,9] result in unphysical predictions: heat capacity that is rising with pressure or negative heat capacity.

respect to its EOS parameters. As explained in Section 3.1, the modelling of magnetic effects in bcc-Fe was done using the standard “magnetic” contribution to the Gibbs free energy [4]. Following Lu et al. [9], the magnetic contribution was left independent of pressure for iron.

The recent assessment by Lu et al. [9] was used as a benchmark for fitting the phase diagram up to $P = 40$ GPa. Above this pressure, the experimental phase diagram data becomes scattered. Here, the shock wave data was used for fitting EOS parameters of the hcp and the liquid phases. Particularly, the onset of melting on the Hugoniot, at $P = 225$ GPa, as observed by Nguyen and Holmes [66], was used to determine the high-pressure liquidus. The result, as seen in Fig. 12, is a rather steep melting curve. The calculated melting temperature at $P = 330$ GPa (the pressure in the inner core boundary of the Earth) is $T = 6700$ K.

The calculated room-temperature compression and principal Hugoniot curve for iron are shown in Fig. 13, with the

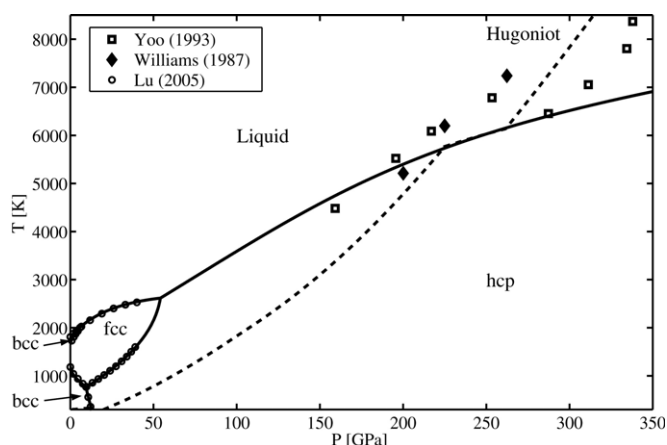


Fig. 12. The phase diagram and the principal Hugoniot of iron in P – T coordinates. The circles represent the assessed phase diagram by Lu et al. [9] that were used for fitting the phase diagrams. The diamonds and the squares represent the shock-temperature measurements by Williams et al. [69] and Yoo et al. [70].

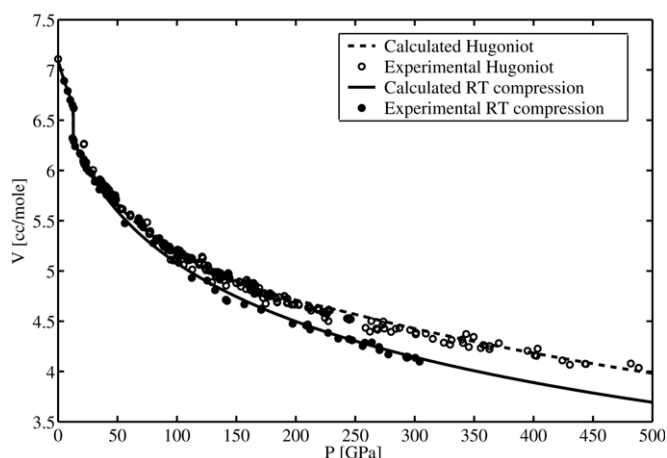


Fig. 13. The room-temperature compression and the Hugoniot curve of iron.

corresponding experimental data [35,54,61]. The quality of the fit may be regarded as satisfactory, at least up to 500 GPa. The calculated Hugoniot is shown also in P – T coordinates in Fig. 12, along with the experimental results by Williams et al. [69] and Yoo et al. [70]. The agreement of the calculation with these results is fair, in view of their large uncertainty.

In Fig. 14, the calculated quantity c_B in Fe, along the Hugoniot curve is compared with the measurements of Altschuler et al. [71] and Brown and McQueen [67]. In the liquid, the calculated sound velocity corresponds to the real acoustic sound velocity. A satisfactory agreement was observed between the calculation and the experimental results that were not used for parameter-fitting.

It should be noted that calculations such as those presented here were never done before in the CALPHAD environment since they were impossible to perform with previous models of $V(T, P)$ used in CALPHAD.¹¹

¹¹ For example, the model of Lu et al. [9] would give imaginary values for the quantity c_B because of the occurrence of negative heat capacities.

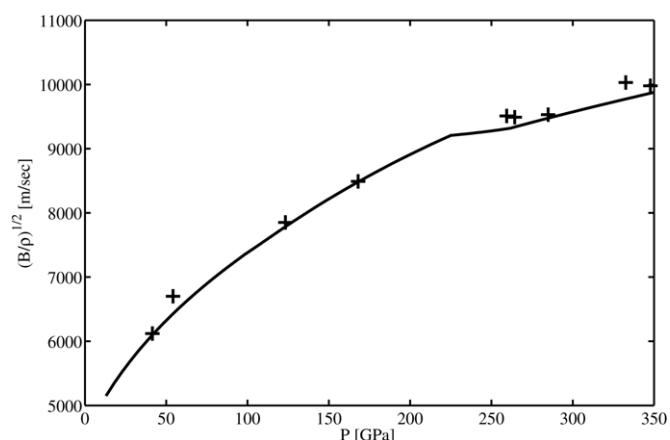


Fig. 14. The calculated quantity $c_B = \sqrt{B_s/\rho}$ in Fe, along the Hugoniot curve is compared with the measurements of Altschuler et al. [71] and Brown and McQueen [67].

4.5. Al–Si

The pressure dependence of the Al–Si alloy system was calculated based on the models generated for Al and Si elements *without any additional parameter fitting*. The interaction coefficients for the fcc and liquid solutions were taken from the SGTE-SSOL database [72] and were left independent of pressure. In the liquid phase, we assumed that the Redlich–Kister parameters in the SSOL database correspond to interactions with the ordinary metallic silicon liquid. It was further assumed that the interaction coefficient between aluminium and the semiconducting liquid species Si^1 is equal to the interaction parameter between the two liquid silicon species. Overall, the introduction of another liquid silicon species and the reassessment of liquid silicon lattice-stability had little effect on the calculated phase diagram at ambient pressure.

The phase diagram of the Al–Si alloy system, calculated at ambient pressure, $P = 2.8$ GPa and at $P = 5.4$ GPa, is shown in Fig. 15 where it is compared with the experimental results [73,74] cited by Murray and McAllister [75]. The calculated liquidus and solidus agree well with the experimental data whereas the calculated solubility of silicon in fcc is seen to be too low, comparing with the corresponding experiment.

In Fig. 16, the eutectic temperature of Al–Si, calculated as function of pressure is shown and compared with the experimental results of Kingon and Clark [76] and Mii et al. [74]. It is encouraging to see that the strange measured maximum of the $T_{\text{Eutectic}}(P)$ curve is reproduced by the calculation (without fitting). Finally, in Fig. 17, the Al–Si phase diagram is calculated at $P = 15$ GPa. It would be interesting to see how far this predicted diagram is from future experiments, or from calculations that are physically well defined.

5. Discussion

The aim of the present work was to improve the predictive power of models accounting for the pressure dependence of the Gibbs free energy, in order to enable the application

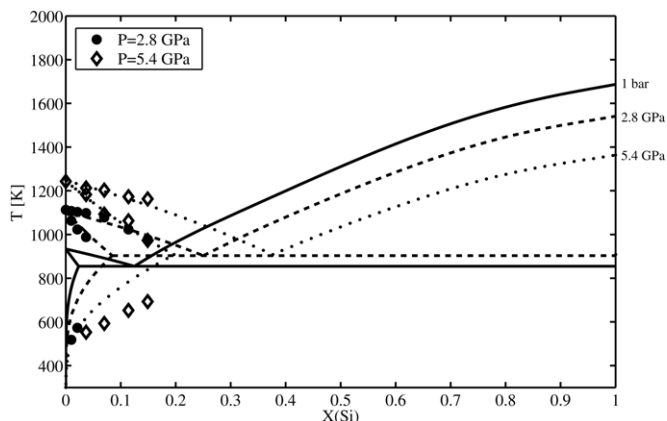


Fig. 15. The phase diagram of the Al-Si alloy system calculated at three pressures, compare with the experimental results of Fujishiro et al. [73] and Mii et al. [74].

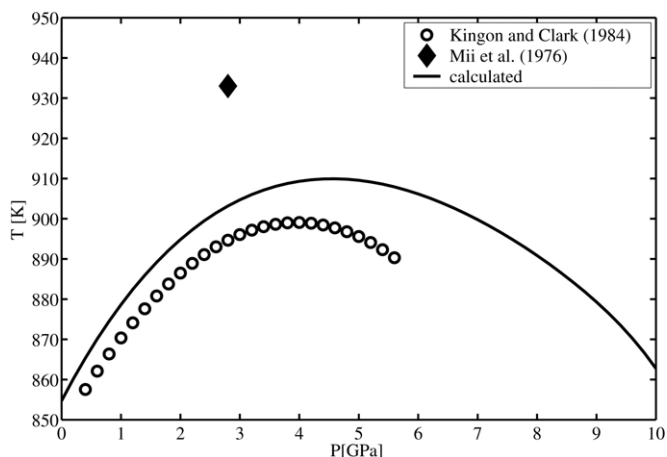


Fig. 16. The eutectic temperature of Al-Si calculated as function of pressure, compared with the experimental results of Kingon and Clark [76] and Mii et al. [74].

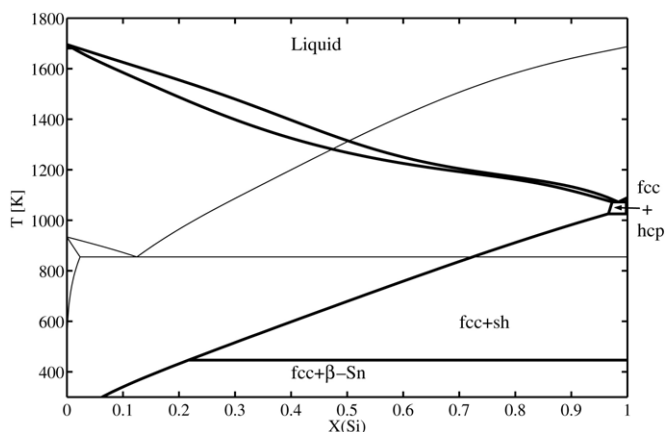


Fig. 17. The phase diagram Al-Si, calculated at 15 GPa (heavy curve). The ambient pressure phase diagram is also drawn for comparison (thin curve).

of CALPHAD at high pressures. Our opinion is that better modelling could be done if the CALPHAD methodology would change towards models that are more physical. As shown in Section 2, this cannot be done just by inserting a physically

derived EOS into CALPHAD calculations. Instead, CALPHAD databases should be completely rewritten, as done by Jacobs et al. [19]. However, this is an enormous task.

Instead, we developed and tested a new EOS that can still achieve a considerable improvement, within the current CALPHAD methodology.

This new formulation is empirical and is not derived from some well defined physical model. However, some problems with existing formulations, such as spurious predictions of negative thermal expansion¹ and negative heat capacity are avoided.

The application of the model to several substances in Sections 4.1–4.5 proves the capability of the model to cope with very high pressures and very high temperatures, as encountered in geophysical systems. No special problems were encountered when fitting the same model for both liquid and solid phases, probably because the difference between the EOS of liquids and solids is accounted for by the $G(T, P_0)$ functions as they are used to calculate $C(T)$.

The implementation of the proposed model is simple. In fact, its implementation in the Thermo-Calc software [22] was done using regular “TCM” and “TDB” files, without modifying the source code. The compatibility of the model with current CALPHAD methodology and SGTE databases facilitates its use for modelling of multi-component systems.

Although the new EOS was tested on an alloy system, the issue of representing the composition dependence of thermophysical properties remains open. We suggest that the best way of doing this type of modelling is by use of pressure-dependent interaction parameters as proposed by Zhao [77], rather than by explicit dependences of the model parameters on composition.

6. Conclusions

It was shown that some of the difficulties encountered in extending CALPHAD to high pressures are the result of an incompatibility between the EOS and the model used for the ambient-pressure heat capacity.

Here, a new free energy formulation, specifically designed for application of the CALPHAD method at high pressures, was developed. This formulation was applied to several typical problems of interest to the CALPHAD community and shows an improvement over previous attempts.

In view of the incompatibility between the CALPHAD approach and physically derived EOS, the present work provides a viable interim solution for many problems that may involve CALPHAD in high-pressure geophysical applications.

Appendix A. Cold compression curve

We suggest that the molar volume at $T = 0$ K $V(0, P)$ may be written as a sum [78]:

$$V(0, P) = \frac{dG_c}{dP} = V_0 \cdot \sum_{n=2}^5 c_n \cdot [X_n(B_0, B'_0, P)]^3 \quad (\text{A.1})$$

where X_n are functions of the pressure, given by:

$$X_n(B_0, B'_0, P) = \left[1 - a_n + a_n \cdot \left(1 + \frac{n}{3a_n} \cdot \frac{P}{B_0} \right)^{\frac{1}{n}} \right]^{-1} \quad (\text{A.2})$$

where $a_n = (n - 1) \cdot (3B'_0 - 1)^{-1}$.

V_0, B_0, B'_0 are the reference molar volume, the bulk modulus and its pressure derivative at $(0, P_0)$.

The coefficients c_n in Eq. (A.1) also depend on material properties V_0, B_0, B'_0 and the atomic numbers Z of the substance components, so that c_n should not be considered as additional adjustable parameters.

In order to satisfy the relation $V(0, P_0) = V_0$, the c_n coefficients are normalized:

$$\sum_{n=2}^5 c_n = 1. \quad (\text{A.3})$$

In order to ensure that the second pressure derivative of the bulk modulus has a reasonable value, the c_n satisfy the equation:

$$9c_5 + 8c_4 + 6c_3 = 8. \quad (\text{A.4})$$

Two more constraints on the c_n coefficients are established by requiring that the EOS should interpolate smoothly with Thomas–Fermi type models at a certain interpolation pressure P_i . In the present work, the calculation by Kalitkin and Kuzmina [79] of the quantum-statistical model (QSM) was used as the high-pressure limit. Following a similar procedure by Kormer and Urlin [80], the requirement for smooth interpolation is given as:

$$V_0 \cdot \sum_{n=2}^5 c_n \cdot [X_n(B_0, B'_0, P_i)]^3 = V_{\text{QSM}}(P_i) \quad (\text{A.5a})$$

$$V_0 \cdot \sum_{n=2}^5 c_n \cdot [X_n(B_0, B'_0, P_i + \Delta P_i)]^3 = V_{\text{QSM}}(P_i + \Delta P_i) \quad (\text{A.5b})$$

where ΔP_i is a relatively small pressure increment.

In the present work the interpolation pressure was chosen to be $P_i = 300$ TPa with $\Delta P_i = 30$ TPa. At this pressure, the QSM is probably quite accurate for any material. Analytic expressions for $V_{\text{QSM}}(P_i)$ and $V_{\text{QSM}}(P_i + \Delta P_i)$, fitted to Kalitkin and Kuzmina [79] are given below:

$$V_{\text{QSM}}(300 \text{ TPa}) = 0.02713 \cdot \exp[0.97626 \cdot (\ln Z) - 0.057848 \cdot (\ln Z)^2] \text{ (cc/mole)} \quad (\text{A.6a})$$

$$V_{\text{QSM}}(330 \text{ TPa}) = 0.025692 \cdot \exp[0.97914 \cdot (\ln Z) - 0.057741 \cdot (\ln Z)^2] \text{ (cc/mole)}. \quad (\text{A.6b})$$

For a compound $A_m B_n$, the volume at a given (high) pressure is

$$V_{\text{QSM}}(A_m B_n) = m \cdot V_{\text{QSM}}(Z_A) + n \cdot V_{\text{QSM}}(Z_B). \quad (\text{A.7})$$

Eq. (A.1) may be integrated to yield a closed-form expression for $G_c(P)$:

$$G_c(P) = B_0 \cdot V_0 \cdot \sum_{n=2}^5 c_n \cdot [\Gamma_n(B'_0, X_n) - \Gamma_n(B'_0, 1)] \quad (\text{A.8})$$

where the functions $\Gamma_n(B'_0, X)$ are defined as:

$$\Gamma_n(B'_0, X) = \frac{3a_n^{(1-n)}}{n} \sum_{k=0}^{k=n} [C_n^k \cdot (a_n - 1)^{n-k} \cdot d_k(X)]. \quad (\text{A.9})$$

X_n also depends on the pressure and the material parameters (B_0, B'_0) according to Eq. (A.2), C_n^k are the binomial coefficients and $d_k(X) = \begin{cases} X^{3-k} \cdot \left(\frac{k}{k-3}\right), & k \neq 3 \\ -3 \ln(X), & k = 3 \end{cases}$.

To summarize this section, the cold compression curve that is proposed here depends on the same adjustable parameters V_0, B_0, B'_0 as other EOS. Its advantages over other formulations are:

1. At very high pressure, the new cold curve uses an interpolation with a physically derived model.
2. The Gibbs free energy is expressed directly as a function of pressure. This should ease the implementation of the new formulation in CALPHAD databases.

Appendix B. Pressure dependence of characteristic temperatures

We suggest the following pressure dependence of θ :

$$\theta = \theta_0 \cdot \exp \left\{ \frac{\gamma_0}{1 + \delta_0} \cdot [\Gamma_2(b_0, X_2^T) - \Gamma_2(b_0, 1)] \right\} \quad (\text{B.1})$$

where $\theta_0, \gamma_0, \delta_0$ and b_0 are adjustable parameters of the EOS. X_2^T depends on the pressure and the parameters $(\frac{B_0}{1+\delta_0}, b_0)$ the same way as X_n depends on (B_0, B'_0) in Eq. (A.2). The superscript “T” is to indicate that the function $X_2^T(\frac{B_0}{1+\delta_0}, b_0, P)$ is related to temperature effects on the EOS.

The effect of the parameters γ_0, δ_0 and b_0 can be evaluated by looking at the volumetric contribution of the QH term — Eq. (6).

At a temperature that is significantly higher than θ , $V^{\text{QH}}(T, P)$ simplifies into:

$$V^{\text{QH}}(T > 2\theta, P) = 3NR T \cdot \frac{d \ln(\theta)}{dP} = T \cdot V_0 \cdot \alpha_0 \cdot (X_2^T)^3 \quad (\text{B.2})$$

where $\alpha_0 = \frac{3NR \cdot \gamma_0}{B_0 \cdot V_0}$ may be identified with the thermal expansion coefficient at ambient pressure and moderate temperatures. Thus, it is visible that the γ_0 factor is related to the Grüneisen parameter.¹²

¹² Note that at high temperature the volumetric contribution has linear temperature dependence. That is $\frac{\partial^2 V^{\text{QH}}}{\partial T^2} = 0$.

Making a series expansion of $V(0, P) + V^{\text{QH}}(T, P)$ in powers of pressure yields:

$$V(0, P) + V^{\text{QH}}(T > 2\theta, P) = (V_0 + T \cdot V_0 \cdot \alpha_0) - V_0 \cdot [1 + T \cdot \alpha_0 \cdot (1 + \delta_0)] \cdot \frac{P}{B_0} + O(P^2). \quad (\text{B.3})$$

From the second term in the expansion, see the temperature dependence of the bulk modulus:

$$B(T > 2\theta, 0) \approx \frac{B_0}{1 + T \cdot \alpha_0 \cdot (1 + \delta_0)} \approx B_0 - B_0 \cdot \delta_0 \cdot \alpha_0 \cdot T. \quad (\text{B.4})$$

Thus, it is seen that the empirical EOS parameter δ_0 approximates the Anderson–Grüneisen parameter δ , defined as [11]:

$$\delta \equiv -\frac{1}{\alpha B} \cdot \left(\frac{\partial B}{\partial T} \right)_P. \quad (\text{B.5})$$

The parameter b_0 in our EOS controls the thermal expansion at high pressure. As may be evaluated from Eq. (B.2), a higher b_0 means that the decrease of the thermal expansion with pressure will be slower. Although b_0 has no direct counterpart in conventional EOS models, its choice may be related to the details of the $\gamma(V)$ function. We suggest that $b_0 = 1$, can be a good starting point for adjusting the b_0 parameter.

Appendix C. Calculation of $C(T)$ with the SGTE database

The definition of $C(T)$ is given in Eq. (7). However, when $G(T, P_0)$ is taken from the SGTE database, there is a problem in calculating $C(T)$ at low temperatures, since the SGTE database is useful only above $T_0 = 298.15$ K. In order to tackle this technical problem, we used the following method for calculating $C(T)$:

$$\begin{aligned} T < T_0, \quad C(T) &= \frac{T^2}{2 \cdot T_0} [C_p^{\text{SGTE}}(T_0) - C_p^{\text{QH}}(T_0)] \\ T \geq T_0, \quad C(T) &= -[G^{\text{SGTE}}(T) - H_{T_0}^{\text{SGTE}} + T \cdot S_{T_0}^{\text{SGTE}}] \\ &\quad + [G^{\text{QH}}(T, P_0) - H_{T_0}^{\text{QH}} + T \cdot S_{T_0}^{\text{QH}}] \\ &\quad + \left(T - \frac{T_0}{2} \right) \cdot [C_p^{\text{SGTE}}(T_0) - C_p^{\text{QH}}(T_0)] \end{aligned} \quad (\text{C.1})$$

where $H_{T_0}^{\text{SGTE}}$, $S_{T_0}^{\text{SGTE}}$ and $C_p^{\text{SGTE}}(T_0)$ are the enthalpy, the entropy and the heat capacity at T_0 calculated from the SGTE database for the modelled phase and $H_{T_0}^{\text{QH}}$, $S_{T_0}^{\text{QH}}$ and $C_p^{\text{QH}}(T_0)$ are these same properties, calculated from the $G^{\text{QH}}(T, P_0)$ function.

Appendix D. The interpolation function $I(P)$

According to Eq. (8), the interpolation term contributes an additional volumetric term:

$$V^{\text{Interp}}(T, P) = -C(T) \cdot \frac{dI(P)}{dP} = C(T) \cdot \frac{(1 + \delta_1)}{B_0(1 + b_1)} \cdot \exp \left\{ \frac{1}{b_1} - \frac{1}{b_1} \cdot \left[1 + 2 \cdot (1 + \delta_1) \cdot \frac{b_1 \cdot P}{B_0} \right]^{\frac{1}{2}} \right\} \quad (\text{D.1})$$

where we choose to give it the form of the pseudospinodal EOS [81], with a pseudocritical exponent $\beta = 1/2$. $\frac{B_0}{1 + \delta_1}$ and b_1 are substituted for the bulk modulus and its pressure derivative at zero pressure, where δ_1 and b_1 are additional adjustable parameters of the EOS.

Thus, the integrated form $I(P)$ is:

$$I(P) = \frac{1}{(1 + b_1)} \cdot \left\{ b_1 + \left[1 + 2 \cdot b_1 \cdot (1 + \delta_1) \cdot \frac{P}{B_0} \right]^{\frac{1}{2}} \right\} \cdot \exp \left\{ \frac{1}{b_1} - \frac{1}{b_1} \cdot \left[1 + 2 \cdot b_1 \cdot (1 + \delta_1) \cdot \frac{P}{B_0} \right]^{\frac{1}{2}} \right\}. \quad (\text{D.2})$$

At zero pressure, the thermal expansion is given by:

$$\begin{aligned} \frac{dV(T > 2\theta, 0)}{V_0 \cdot dT} &= \alpha_0 + \frac{dC(T)}{dT} \cdot \frac{(1 + \delta_1)}{B_0 \cdot V_0 \cdot (1 + b_1)} \\ &= \alpha_0 + \alpha_1 \end{aligned} \quad (\text{D.3})$$

where $\alpha_1 = \frac{dC(T)}{dT} \cdot \frac{(1 + \delta_1)}{B_0 \cdot V_0 \cdot (1 + b_1)}$.

Thus, it is seen that with higher values of δ_1 and lower values of b_1 , there is a larger volumetric contribution of the interpolation term at zero pressure.

The parameter b_1 affects the thermal expansion and the heat capacity at high temperatures, similarly to the parameter b_0 in the QH term.

The notation used for the δ_1 parameter is clarified by performing a derivation similar to Eq. (B.4) but this time with the interpolation term. The result, parallel to Eq. (B.4) is

$$B(T > 2\theta, 0) \approx B_0 - B_0 \cdot \delta_0 \cdot \alpha_0 \cdot T - B_0 \cdot \delta_1 \cdot \alpha_1 \cdot T \quad (\text{D.4})$$

where the resemblance between the role of δ_1 and that of δ_0 in Eq. (D.4) may be appreciated.

Finally, note that because $\frac{d^2C(T)}{dT^2} > 0$, the volumetric contribution of the interpolation term is dominant at high temperatures and low pressures. Therefore, at very high temperature the calculated bulk modulus converges to the bulk modulus of the interpolation term $\frac{B_0}{1 + \delta_1}$, avoiding the spinodal mechanical instability.

References

- [1] O.B. Fabrichnaya, S.K. Saxena, Thermodynamic Data, Models, and Phase Diagrams in Multicomponent Oxide Systems, Springer, 2004.
- [2] X.G. Lu, M. Selleby, B. Sundman, CALPHAD 29 (2005) 68–89.
- [3] X.G. Lu, M. Selleby, B. Sundman, Acta Mater. 53 (2005) 2259–2272.
- [4] A.T. Dinsdale, CALPHAD 15 (1991) 317–425.
- [5] A.F. Guillermet, P. Gustafson, M. Hillert, J. Phys. Chem. Solids 46 (1985) 1427–1429.
- [6] A.F. Guillermet, Internat. J. Thermophys. 16 (1995) 1009–1026.
- [7] S.K. Saxena, Geochim. Cosmochim. Acta 60 (1996) 2379–2395.
- [8] M.H.G. Jacobs, H.A.J. Oonk, CALPHAD 24 (2000) 133–147.
- [9] X.G. Lu, M. Selleby, B. Sundman, CALPHAD 29 (2005) 49–55.
- [10] A.F. Guillermet, Internat. J. Thermophys. 6 (1985) 367–393.
- [11] O.L. Anderson, Equations of State of Solids for Geophysics and Ceramic Science, Oxford University Press, Oxford, 1995.
- [12] A. Hänström, P. Lazor, J. Alloys Compd. 305 (2000) 209–215.

- [13] P.D. Desai, *Internat. J. Thermophys.* 8 (1987) 621–638.
- [14] J.O. Anderson, A.F. Guillermet, P. Gustafson, M. Hillert, B. Jansson, B. Jönsson, B. Sundman, J. Ågren, *CALPHAD* 11 (1987) 93–98.
- [15] G. Grimvall, *Berichte Der Bunsen-Gesellschaft-Physical Chemistry Chemical Physics* 102 (1998) 1083–1087.
- [16] P.G. Debenedetti, *Metastable Liquids, Concepts and Principles*, Princeton University Press, Princeton, New-Jersey, 1996.
- [17] E. Brosh, G. Makov, R.Z. Shneck, *J. Phys.: Condens. Matter* 15 (2003) 2991–3001.
- [18] Y. Wang, S. Curtarolo, C. Jiang, R. Arroyave, T. Wang, G. Ceder, L.-Q. Chen, Z.-K. Liu, *CALPHAD* 28 (2004) 79–90.
- [19] M.H.G. Jacobs, A.P. van den Berg, B.H.W.S. de Jong, *CALPHAD* 30 (2006) 131–146.
- [20] T.V. Gerya, K.K. Podlesskii, L.L. Perchukand, W.V. Maresh, *Phys. Chem. Miner.* 31 (2004) 429–455.
- [21] J. Ågren, *Phys. Chem. Liquids* 18 (1988) 123–139.
- [22] J.O. Andersson, T. Helander, L.H. Höglund, P.F. Shi, B. Sundman, *CALPHAD* 26 (2002) 273–312.
- [23] Y.S. Touloukian, R.K. Kirby, R.E. Taylor, P.D. Desai, *Thermal Expansion, in: Thermophysical Properties of Matter*, vol. 12, Plenum Press, New York, 1975.
- [24] K. Syassen, W.B. Holzapfel, *J. Appl. Phys.* 49 (1978) 4427–4430.
- [25] Z. Chubin, L. Shaomeng, T. Yagang, *J. Phys. Chem. Solids* 58 (1997) 835–838.
- [26] R.G. Greene, H. Luo, A.L. Ruoff, *Phys. Rev. Lett.* 73 (1994) 2075–2077.
- [27] J.L. Tallon, W. Wolfenden, *J. Phys. Chem. Solids* 40 (1979) 831–837.
- [28] G. Gerlich, E.S. Fisher, *J. Phys. Chem. Solids* 30 (1969) 1197–1205.
- [29] P.S. Ho, A.L. Ruoff, *J. Appl. Phys.* 40 (1969) 3151–3156.
- [30] N.M. Kéita, S. Steinmann, *J. Phys. C: Solid State Phys.* 11 (1978) 4635–4641.
- [31] V. Sarou-Kanian, F. Millot, J.C. Rifflet, *Internat. J. Thermophys.* 24 (2003) 277–286.
- [32] R. Boehler, M. Ross, *Earth Planet. Sci. Lett.* 153 (1997) 223–227.
- [33] J.L. Pélissier, *Physica A* 128 (1984) 363–370.
- [34] G.R. Gathers, *Rep. Progr. Phys.* 49 (1986) 341–396.
- [35] Russian Foundation for Basic Research, Shock-Wave database. <http://teos.ficp.ac.ru/rusbank>, <http://ns.ihed.ras.ru/rusbank>.
- [36] J.W. Shaner, J.M. Brown, R.G. McQueen, *Mat. Res. Soc. Symp. Proc.* 22 (1984) 137–141.
- [37] Y.S. Touloukian, R.K. Kirby, R.E. Taylor, T.Y.R. Lee, *Thermal Expansion, in: Thermophysical Properties of Matter*, vol. 13, Plenum Press, New York, 1977.
- [38] H.J. McSkimin, *J. Appl. Phys.* 24 (1953) 988–997.
- [39] H.J. McSkimin, P. Andreatch Jr., *J. Appl. Phys.* 35 (1964) 2161–2165.
- [40] S. Rajagopalan, *II Nuovo Chimento* 51B (1979) 222–228.
- [41] H. Olijnyk, S.K. Sikka, W.B. Holzapfel, *Phys. Lett.* 103A (1984) 137–140.
- [42] S.J. Duclos, Y.K. Vohra, A.L. Ruoff, *Phys. Rev. B* 41 (1990) 12021–12028.
- [43] W.K. Rhim, S.K. Chung, A.J. Rulison, R.J. Spjut, *Internat. J. Thermophys.* 18 (1997) 459–469.
- [44] N.M. Kéita, S. Steinmann, *Phys. Lett.* 72A (1979) 153–154.
- [45] G.A. Voronin, C. Pantea, T.W. Zerda, L. Wang, Y. Zhao, *Phys. Rev. B* 68 (2003) 020102.
- [46] M.T. Yin, M.L. Cohen, *Phys. Rev. B* 26 (1982) 5668–5687.
- [47] K.J. Chang, M.L. Cohen, *Phys. Rev. B* 31 (1985) 7819–7826.
- [48] H. Tanaka, *Phys. Rev. B* 66 (2002) 064202.
- [49] S.K. Deb, M. Wilding, M. Somayazulu, P.F. McMillan, *Nature* 414 (2001) 528–530.
- [50] S. Stølen, T. Grande, *Thermodynamics of Materials: Macroscopic and Microscopic Aspects*, Wiley, 2004, pp. 143–149.
- [51] J.L. Feldman, J.Q. Broughton, F. Wooten, *Phys. Rev. B* 43 (1991) 2152–2158.
- [52] L.S. Dubrovinsky, S.K. Saxena, *Phys. Chem. Miner.* 24 (1997) 547–550.
- [53] D.G. Isaak, O.L. Anderson, T. Goto, *Phys. Chem. Miner.* 16 (1989) 704–713.
- [54] H.K. Mao, P.M. Bell, *J. Geophys. Res.* 84 (1979) 4533–4536.
- [55] K. Wang, R.R. Reeber, *Geophys. Res. Lett.* 22 (1995) 1297–1300.
- [56] H. Cynn, O.L. Anderson, D.G. Isaak, M. Nicol, *J. Phys. Chem.* 99 (1995) 7813–7818.
- [57] A.F. Guillermet, P. Gustafson, *High Temp.-High Pressures* 16 (1985) 691–710.
- [58] D.G. Isaak, K. Masuda, *J. Geophys. Res.* 100 (1995) 17,689–17,698.
- [59] H.K. Mao, W.A. Basset, T. Takahashi, *J. Appl. Phys.* 38 (1967) 272–276.
- [60] D.J. Dever, *J. Appl. Phys.* 43 (1972) 3293–3301.
- [61] H.K. Mao, Y. Wu, L.C. Chen, J.F. Shu, *J. Geophys. Res.* 95 (1990) 21,737–21,742.
- [62] T. Uchida, Y. Wang, M.L. Rivers, S.R. Sutton, *J. Geophys. Res.* 106 (2001) 21,799–21,810.
- [63] R. Bohler, N. von Barga, A. Chopleas, *J. Geophys. Res.* 95 (1990) 21,731–21,736.
- [64] R.S. Hixon, M.A. Winkler, M.L. Hodgdon, *Phys. Rev. B* 42 (1990) 6485–6491.
- [65] M. Beutl, G. Pottlacher, H. Jager, *Internat. J. Thermophys.* 15 (1994) 1323–1331.
- [66] J.H. Nguyen, N.C. Holmes, *Nature* 427 (2004) 339–342.
- [67] J.M. Brown, R.G. McQueen, *J. Geophys. Res. Ser. B* 91 (1986) 7485–7494.
- [68] O.L. Anderson, D.G. Isaak, *Amer. Miner.* 85 (2000) 376–385.
- [69] Q. Williams, R. Jeanvendsen, T. Ahrens, *Science* 236 (1987) 181–182.
- [70] C.S. Yoo, N.C. Holmes, M. Ross, D.J. Webb, C. Pike, *Phys. Rev. Lett.* 70 (1993) 3931–3934.
- [71] L.V. Altshuler, S.B. Kormer, M.I. Brazhnik, L.A. Vladimirov, M.P. Speranskaya, A.I. Funtikov, *Sov. Phys. JETP* 11 (1960) 766–775.
- [72] SGTE – SSOL4, 2005.
- [73] I. Fujishiro, H. Mii, M. Senoo, M. Akao, *J. Soc. Mater. Sci. Jpn.* 20 (1971) 952–955.
- [74] H. Mii, M. Senoo, I. Fujishiro, *Jpn. J. Appl. Phys.* 15 (1976) 777–783.
- [75] J.L. Murray, A.J. McAllister, *Bull. Alloy Phase Diagrams* 5 (1984) 74–84.
- [76] A.I. Kingon, J.S.B. Clark, *High Temp.-High Pressures* 16 (1984) 137–141.
- [77] M. Zhao, *The Theory and Calculation of P - T - X_i Multicomponent Phase Diagrams*, Nova Science publishers, New-York, 1996.
- [78] E. Brosh, G. Makov, R.Z. Shneck, *J. Nucl. Mater.* 344 (2005) 36–39.
- [79] N.N. Kalitkin, L.V. Kuzmina, *Sov. Phys. Solid State* 13 (1972) 1938–1942.
- [80] S.B. Kormer, V.D. Uralin, *Sov. Phys. Dokl.* 5 (1960) 317–320.
- [81] V.G. Baonza, M. Cáceres, J. Núñez, *Phys. Rev. B* 51 (1995) 28–37.